Correlating laser energy with compositional and atomic-level information of oxides in atom probe tomography

Journal Article

Author(s):
Hunnestad, Kasper A.; Hatzoglou, Constantinos; Vurpillot, François; Nylund, Inger E.; Yan, Zewu (iD); Bourret, Edith; van Helvoort, Antonius T.J.; Meier, Dennis
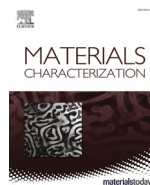
Correlating laser energy with compositional and atomic-level information of oxides in atom probe tomography

K.A. Hunnestad [a], C. Hatzoglou [a], F. Vurpillot [b], I.-E. Nylund [a], Z. Yan [c,d], E. Bourret [d], A.T.J. van Helvoort [e], D. Meier [a,*]

[a] Department of Materials Science and Engineering, Norwegian University of Science and Technology (NTNU), 7491 Trondheim, Norway
[b] UNIROUEN, CNRS, Groupe de Physique des Matériaux, Normandie Université, Av. de l'Université BP12, 76801 St Etienne du Rouvray, France
[c] Department of Physics, ETH Zurich, Zürich, Switzerland
[d] Materials Sciences Division, Lawrence Berkeley National Laboratory, Berkeley, CA, USA
[e] Department of Physics, Norwegian University of Science and Technology (NTNU), 7491 Trondheim, Norway

ARTICLE INFO

ABSTRACT

Atom probe tomography (APT) is a 3D analysis technique that offers unique chemical accuracy and sensitivity with sub-nanometer spatial resolution. There is an increasing interest in the application of APT to complex oxides materials, giving new insight into the relation between local variations in chemical composition and emergent physical properties. However, in contrast to the field of metallurgy, where APT is routinely applied to study materials at the atomic level, complex oxides and their specific field evaporation mechanisms are much less explored. Here, we perform APT measurements on the hexagonal manganite $ErMnO_3$ and systematically study the effect of different experimental parameters on the measured composition and structure. We demonstrate that both the mass resolving power (MRP) and compositional accuracy can be improved by increasing the charge-state ratio (CSR) working at low laser energy (< 5 pJ) for a given fixed detection rate. Furthermore, we observe a substantial preferential retention of Er atoms, which is suppressed at higher CSRs. We explain our findings based on fundamental field evaporation concepts, expanding the knowledge about the impact of key experimental parameters and the field evaporation process in complex oxides in general.

1. Introduction

Laser-assisted atom probe tomography (APT) is a well-established characterization technique in metallurgy, where it enabled numerous breakthroughs, shaping, e.g., the modern understanding of clustering and chemical segregation [1,2]. In addition, APT was applied to a range of material systems and geometries, ranging from frozen water [3] to human enamel [4], showing its broad application potential. Recently, there is an increasing interest in measurements on oxide materials, as APT can provide unprecedented insight into key characteristics, such as compositional variations, dopant distributions and defects, that underpin their functional properties. For example, APT has been applied with great success in geosciences to quantify chemical segregation and trace impurities that are mobile on geological timescales [5], to analyze site-specific doping in oxide semiconductors [6], and to investigate the correlation between polar discontinuities and chemical composition at grain boundaries in ferroelectric polycrystals [7]. Furthermore, APT has

been used to access chemical disorder at the atomic level [6,8–11], holding great potential for future studies of emergent phenomena in complex oxides.

Despite the remarkable opportunities, APT measurements also impose different challenges and a range of evaporation artefacts can arise, leading to systematic biases, such as preferential evaporation, preferential retention, co-evaporation, and molecular dissociation [12–17]. These effects can obscure the data analysis, resulting in, e.g., inaccurate compositional measurements, loss of information, or spatial aberrations. To achieve accurate chemical measurements, it is crucial to optimize the experimental parameters; this includes the base temperature, detection rate, laser energy and pulse frequency, as well as the geometry of the sample under investigation (radius and shank angle), which controls the electric field strength at the surface and, hence, the evaporation mechanisms. The importance of the experimental parameters is reflected by several studies, which investigated their influence on the data quality and chemical bias [5,12,13,18–32]. The laser energy

determines the change in temperature during pulsing and is varied to meet the field evaporation criteria for all elements. For many materials, including metals, a laser energy in the range of 30–100 pJ has been demonstrated to be adequate. The base temperature is usually set as low as possible to minimize thermal effects, and high laser frequencies and detection rates are favorable in order to reduce unwanted evaporation events between pulses. As higher temperatures reduce the electric field required for field evaporation, the charge-state ratio (CSR) of a selected ionic species is often used as an indicator for the electric field strength at the apex. The CSR depends on different analysis parameters that are crucial for the field evaporation (e.g., tip geometry, base temperature, laser pulse energy, and detection rate) and, hence, represents an important metric for understanding field evaporation processes [33]. Along with the other experimental parameters, the CSR is typically optimized so that the APT analysis yields an accurate composition measurement for a selected reference system, as well as sharp peaks in the mass spectrum to achieve optimal mass resolving power (MRP).

Interestingly, several oxides have been reported to exhibit a completely different trend with respect to the common analysis parameters and the best results were achieved with low instead of high laser energies (sometimes as low as 0.2 pJ) [34–37]. One reason for this is the low thermal conductivity generally found in oxides, which leads to so-called thermal tails in the mass spectrum. The latter can be minimized by decreasing the laser pulse energy. Furthermore, neutral O_2 molecules can be desorbed on the surface and not subsequently ionization, which usually goes undetected and leads to a loss of information and apparent oxygen deficiency [14] (note this is a complex topic and other suggestions including molecular dissociation have been proposed to explain the loss of oxygen [15,14,39,40]). In both cases, a lower laser energy is beneficial as it increases the CSR and thus the ionization probability of neutral O_2 molecules. It should also be noted that low laser pulse energies simultaneously lead to higher background levels and increased multiple evaporation events, which must be weighed against the positive trade-offs [32]. So far, however, the effect of very low pulse energies in APT measurements has been investigated only in a limited number of oxide materials. In addition, comprehensive investigations concerning the impact on the spatial resolution and atomic imaging in oxide materials are scarce.

Here, we perform a systematic analysis using hexagonal erbium manganite ($ErMnO_3$), monitoring how different APT experimental parameters affect the measurement. $ErMnO_3$ has been intensively studied for its multiferroicity [42–44] and unusual ferroelectric domain wall properties [45,46]. Its atomic structure is well known [47–49], making it an ideal model system. The unit cell consists of alternating Mn and Er lattice planes with a spacing of 5.71 Å along the [001] zone axis, which can readily be resolved by APT [6]. We investigate the effect of the laser energy on the MRP and the measured composition, showing that lower laser energies and higher CSR yield better results, consistent with previous observations on other oxide systems. Going beyond compositional analysis on the bulk level, we demonstrate that variations in CSR (or laser energy) cause substantial variations in the measured distances between the atomic planes of Er and Mn. This CSR-dependent atomic offset is explained based on the preferential retention of Er atoms and changes in specimen temperature, giving new insight into the field evaporation process in complex oxides.

2. Material and methods

The single crystals of $ErMnO_3$ (space group $P6_3cm$) used in this study are grown by the pressurized floating-zone method [50]. Samples are first cut from a larger crystal and then oriented by Laue diffraction to gain surfaces perpendicular to the hexagonal c-axis of the material. A Helios NanoLab DualBeam focused ion beam (FIB) with a Ga source is used to prepare APT needle specimens from the bulk samples as described in Ref. [51].

High-resolution scanning transmission electron microscopy (STEM)

data is taken using a JEOL JEM ARM200F operating at 200 kV. Sample checks and diffraction measurements are taken with a JEOL JEM-2100F Field Emission Electron Microscope, also operated at 200 kV. All TEM data is obtained directly from the APT specimens with no further sample preparation before the APT analysis.

APT analysis is done with a Cameca LEAP 5000XS, operated in laser pulsing mode with a pulsing frequency of 250 kHz and detection rate at 0.5 % (i.e., 1 atom detected on average every 200 laser pulse). The base temperature is either 25 K or 50 K as detailed in the figure captions and the laser energy is set to 5 pJ unless specified differently. To reconstruct the raw APT data into 3D datasets, the software Cameca IVAS 3.6.12 is used. Radius evolution is determined based on the voltage profile and correct reconstruction parameters are found by measuring the plane-to-plane distances along the (001) pole. Typically, an image compression factor of 1.8 is used and a field reduction factor of 2.7 with 30 V/nm as the evaporation field (as for bulk Mn). MRP values are obtained from AP Suite Software 6.1 by calculating $M/\Delta M$, where ΔM is the full width at half maximum (FWHM) of the Mn peak in the mass spectrum [52]. MRP series are obtained by starting at low laser energies and increasing, to reduce the effect of simultaneous increasing radius. Each data point was calculated from a dataset containing around 5-7 M ions. For the SDM analysis we use the Norwegian Atom Probe App (NAPA) software [53], developed in MATLAB®, which calculates the SDM along the direction normal to the atomic planes for best signal-to-noise ratio.

3. Results and discussion

3.1. Sample preparation

A representative FIB-cut $ErMnO_3$ specimen as used for the APT analysis is shown in Fig. 1(a). TEM is applied to verify structural integrity after FIB preparation. Fig. 1(b) presents a high-angle annular dark-field scanning TEM (HAADF-STEM) lattice image gained at the tip of the needle, showing the alternating atomic planes of Er and Mn with the characteristic up-up-down displacement of the Er atoms [46,54,55] in the [100] direction. Note that the up-up-down displacements correspond to the direction of polarization, which is a reversible property in $ErMnO_3$ under the influence of strong electric fields [57]. Only a thin amorphous layer with a thickness of about 10 nm is observed (not shown) on the outside of the needle specimen. In Fig. 1(c), a selected area electron diffraction (SAED) pattern is displayed, corresponding to the whole tip volume; only Bragg reflections associated with the [100] zone axis are observed, excluding any FIB-induced secondary phases. The characteristic needle shape of the specimens is necessary to focus the electric field at the tip and achieve the field strength required for field evaporation (typically around 30 V/nm in APT). Following the field evaporation of the region of interest, the final 3D chemical map in Fig. 1 (d) is then obtained after reconstruction.

3.2. Parameter optimization

For achieving optimal experimental conditions in APT, the laser energy is critical. Its influence on the MRP can be seen in Fig. 2(a), where parts of the mass spectrum are shown with two laser energies (5 pJ and 30 pJ) under a constant detection rate (hence different voltage). The peaks are narrower for the lower laser energy, indicating a higher MRP and, hence, more accurate chemical quantification and sensitivity. We also note that hydrogen related peaks (HO^+ and HMn^{2+}) are significantly reduced, consistent with previous reports [58]. In Fig. 2(b), it is shown in more detail that lower laser energies (≈ 10 pJ) indeed result in higher MRP. Furthermore, it is shown in Fig. 2(c) that the CSR of the ErO species $\left(\frac{ErO^{2+}}{ErO^{2+}+ErO^+}\right)$ increases from 0.2 to 0.9 when decreasing the laser energy from 200 pJ to 0.2 pJ [59]. This change in CSR is also reflected in the measured composition as seen in Fig. 2(d). For higher CSR, the composition approaches the nominal values of 20 % Er, 20 % Mn, and 60
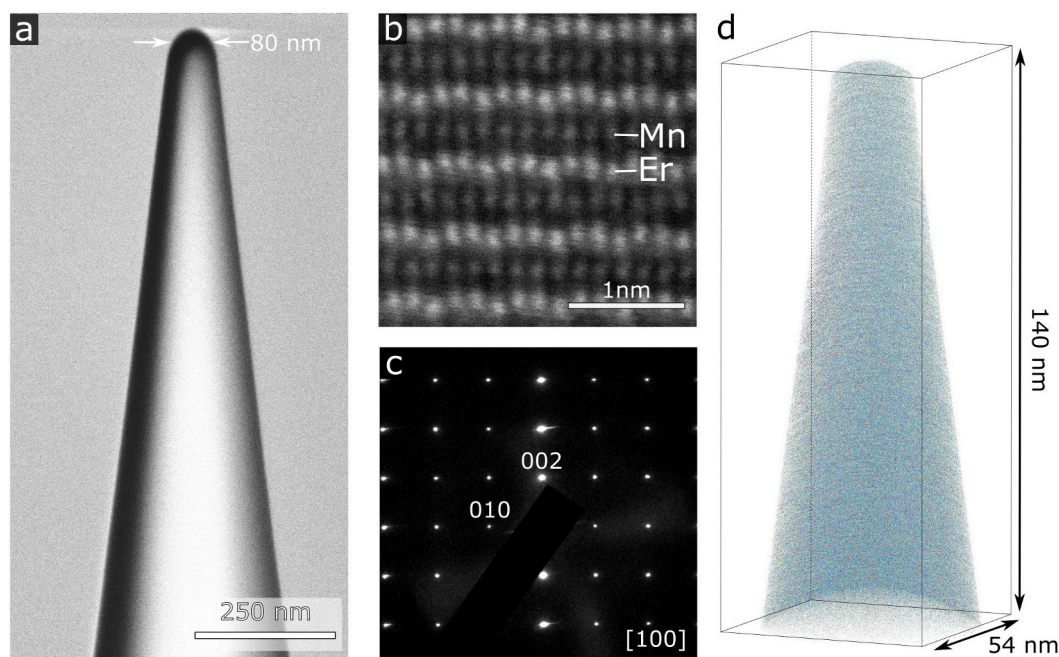
Fig. 1. Sample preparation and atom probe tomography on ErMnO₃. (a) Scanning electron microscopy (SEM) image of an ErMnO₃ APT specimen, shaped into a nanoscale needle using a FIB. (b) HAADF-STEM lattice image showing alternating Er and Mn planes and (c) SAED pattern obtained from the tip of an APT needle, indicating crystallinity. Data is taken along the [100] zone axis. (d) 3D virtual specimen obtained after reconstructing the raw data from the field evaporation. O atoms are colored blue, Mn yellow and Er red. (For interpretation of the references to colour in this figure legend, the reader is referred to the web version of this article.)

% O. Note that the data in each of the plots in Fig. 2(b)–(d) are obtained from three different specimens to exclude bias from a specific sample geometry.

The trend we observe in our APT measurements on ErMnO₃ is consistent with previous reports on other oxide materials, that is, for high CSR and, thus, high electric field strength at the surface, the measured oxygen concentration is higher [60]. This is either due to molecular dissociation or thermal desorption of neutral O₂ molecules which are undetectable in the experiment. To investigate this further, correlation histograms are calculated in Fig. S2 and Fig. S3, where only a few traces of molecular dissociation are found. Thus, in this case thermal desorption appears to be the dominating form of oxygen loss. Furthermore, the Mn concentration drops below the Er concentration, possibly due to preferential evaporation of Mn or molecular dissociation.

3.3. Crystallographic poles and atomic resolution

Some materials form facets perpendicular to a zone axis on the surface of the APT needle during evaporation. These regions, called crystallographic poles, facilitate excellent spatial resolution and can be used to visualize the atomic planes along the zone axis of the pole. In the case of oriented ErMnO₃, a pole is observed along the [001] zone axis as displayed in Fig. 3(a), which corresponds to a 2D slice of the APT dataset. Fig. 3(b) presents the atomic planes of Mn. In Fig. 3(c), a profile across the pole of the composition is shown; the data shows that there is a clear chemical bias in the pole region. This bias could arise for several reasons, such as surface migration or different field conditions at the pole [61,62].

In the pole region, the atomic planes of the different elements can be resolved as summarized in Fig. 4(a)-(c). While the O planes are not directly visible, the alternating planes of Mn and Er are readily resolved, consistent with the HAADF-STEM data in Fig. 1(b) (Fig. 4(d) shows a schematic illustration). For a more quantitative analysis, spatial distribution maps (SDMs) are calculated for all the elements using the Mn ions as reference (Fig. 4(e)) [63]. Because ions of the same type have

overlapping atomic planes, the Mn – Mn SDM can be used to probe the plane-to-plane distance and calibrate the reconstruction so that the distance becomes equal to $d_{Mn} = 5.7$ Å. The Mn – O SDM is not shown as it reflects the evaporation conditions rather than the actual positions; O close to the Er planes tend to evaporate as ErO species, whereas O from the Mn planes evaporate as O. Finally, when considering the Mn – Er SDM, we find that the peaks are located between the Mn planes as we expect from the unit cell structure. When analyzing the exact position more carefully, however, we find a deviation of about 0.04 d_{Mn} from the established position of the Er layer [64].

3.4. Atomic planes offset

An offset with respect to the expected position of atomic planes was observed previously for one-phase binary alloys as discussed in Ref. [64]. During an APT experiment, the evaporation sequence and surface roughness is modified by the individual species' evaporation field. Species that are evaporated later (preferential retention) or earlier than expected are assigned a spatial coordinate along the evaporation direction with a certain offset during the reconstruction [20]. When considering atomic planes such as Er and Mn planes, there will then be an offset between the two atomic planes as demonstrated in Fig. 4, should the two ions have a difference in evaporation field.

To better understand this phenomenon of the Mn – Er offset observed in the SDMs, we analyze the effect of varying electric field strength represented by the CSR. The change in electric field strength is achieved by varying the laser pulse energy as shown in Fig. 5. The data shows a clear trend, approaching the expected Mn – Er offset of 0.5 d_{Mn} with increasing CSR. In contrast, as the CSR decreases (increasing laser energy and temperature), the offset is reduced and the measured location of the Er planes approaches that of the Mn planes. In other words, the spatial offset in Fig. 5 originating from evaporation field differences is shown to depend on the laser energy, which we will elaborate on in the following using fundamental concepts of field evaporation.

In general, the evaporation rate constants (evaporated atoms per unit
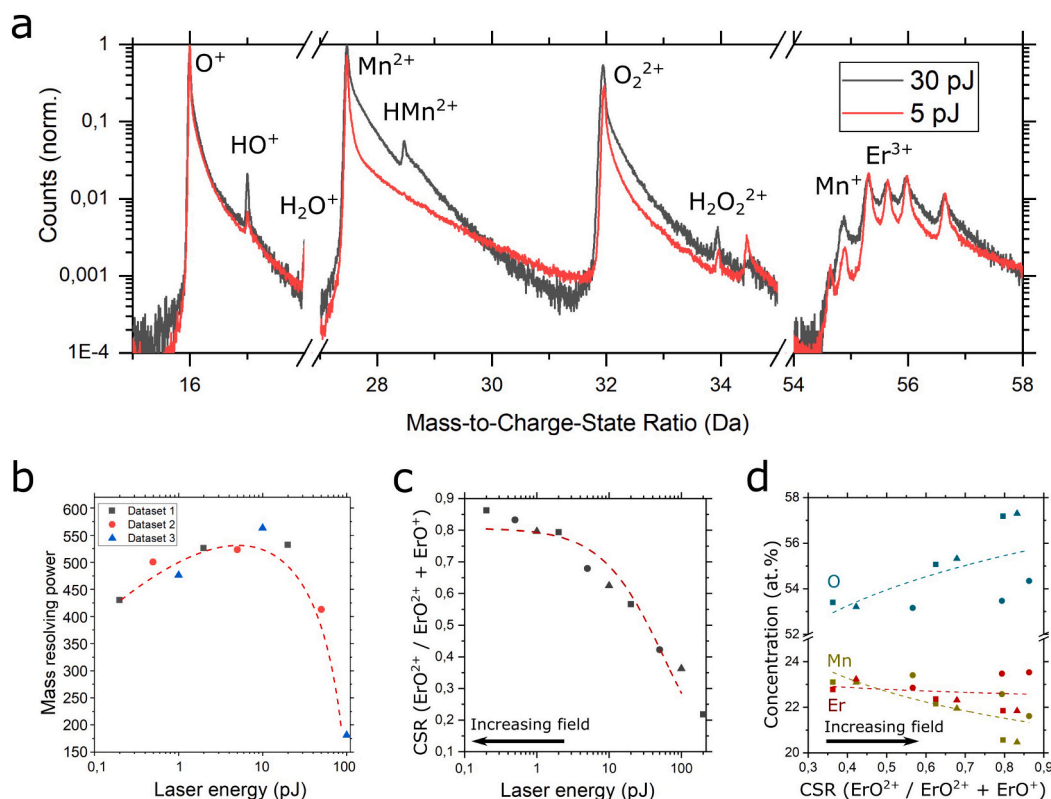
Fig. 2. Influence of the laser energy on key analysis metrics. (a) Mass spectrum of ErMnO$_3$ for two different laser energies, 5 pJ and 30 pJ (see Fig. S4 for a full spectrum). Thermal tails are reduced at 5 pJ compared to 30 pJ. (b) MRP as a function of the laser energy from three different APT specimens (distinguished by colors). All data is acquired under the same parameters aside from the laser energy (i.e. base temperature: 50 K, detection rate: 0.5 %, pulse frequency: 250 kHz). (c) CSR evolution of the ErO ionic species (ErO^{2+} and ErO$^+$) as a function of the laser energy. (d) Composition of the full data volume as a function of CSR. Increasing CSR corresponds to reducing the laser energy. In both (c) and (d) the arrow indicates the direction of which the electric field strength increases, and the plotted lines are guides to the eye. All three plots (b-d) show that analysis conditions are improved towards lower laser energies (<10 pJ).
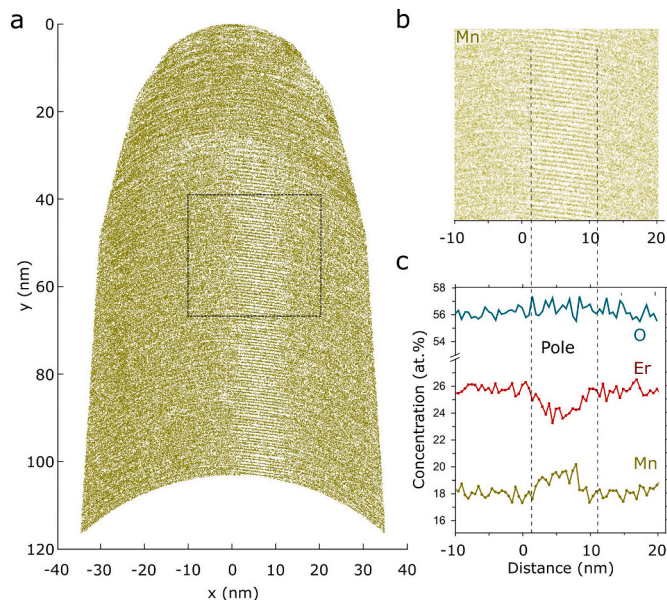
Fig. 3. Influence of the crystallographic pole on the chemical composition. (a) Slice of the full dataset containing the pole, where only the Mn ions are displayed. (b) Smaller region of interest containing the pole, corresponding to the position marked in (a). (c) The chemical composition measured from left to right in the region seen in (b) is shown. A chemical bias around the pole can be seen through an increase in Mn concentration and a decrease in Er concentration. The data is taken at 25 K.

time and atoms) of Er (K_{Er}) and Mn (K_{Mn}) need to be equal in order to obtain a stationary state (i.e., $K_{Er} = K_{Mn} = \gamma$ with γ a constant) and can be defined by an Arrhenius expression [61,65]:

$$K_i = A_i exp\left(-\frac{Q_i\left(F_{T,i}\right)}{k_{\mathrm{B}}T}\right) \qquad (1)$$

with i the considered atoms (Er or Mn), k_{B} the Boltzmann constant, T the temperature at the sample surface and Q_i the energy barrier for an atom i at the electric field $F_{T,i}$. This field represents the total electric field above atom i at evaporation and is referred to as the effective evaporation field. The temperature at the sample surface is equal to the analysis temperature T_0 (i.e., 25 K or 50 K, see Section 2), in addition to the increase in temperature induced by the laser ΔT. The latter is increasingly important as the laser energy increases. At zero temperature, the value of the electric field at which the energy barrier (Q_i) of a specific element is reduced to zero is called the evaporation field ($F_{Ev,i}$). Close to the evaporation field of an atom i, the energy barrier is approximated by the expression:

$$Q_i\left(F_{T,i}\right) = C_i\left(1 - \frac{F_{T,i}}{F_{Ev,i}}\right) \qquad (2)$$

Here, C_i is an energetic constant associated with atom i [66–68]. Experimentally, the linearity of $Q_i(F)$ is approximately observed for some materials in the range of 0.8 $F_{Ev,i}$ to 0.95 $F_{Ev,i}$ [69]. Deviations exist outside this regime (i.e., at high laser energy and low $F_{T,i}$), which we neglected in our approach. The energetic constant C_i is a extrapolation of $Q_i(F_i)$ to zero temperature, assuming a linear approximation of $Q_i(F_i)$, which is valid for fields close to the evaporation field $F_{Ev,i}$. Its value depends on the specific atom (i.e., Mn or Er), but also on the material's
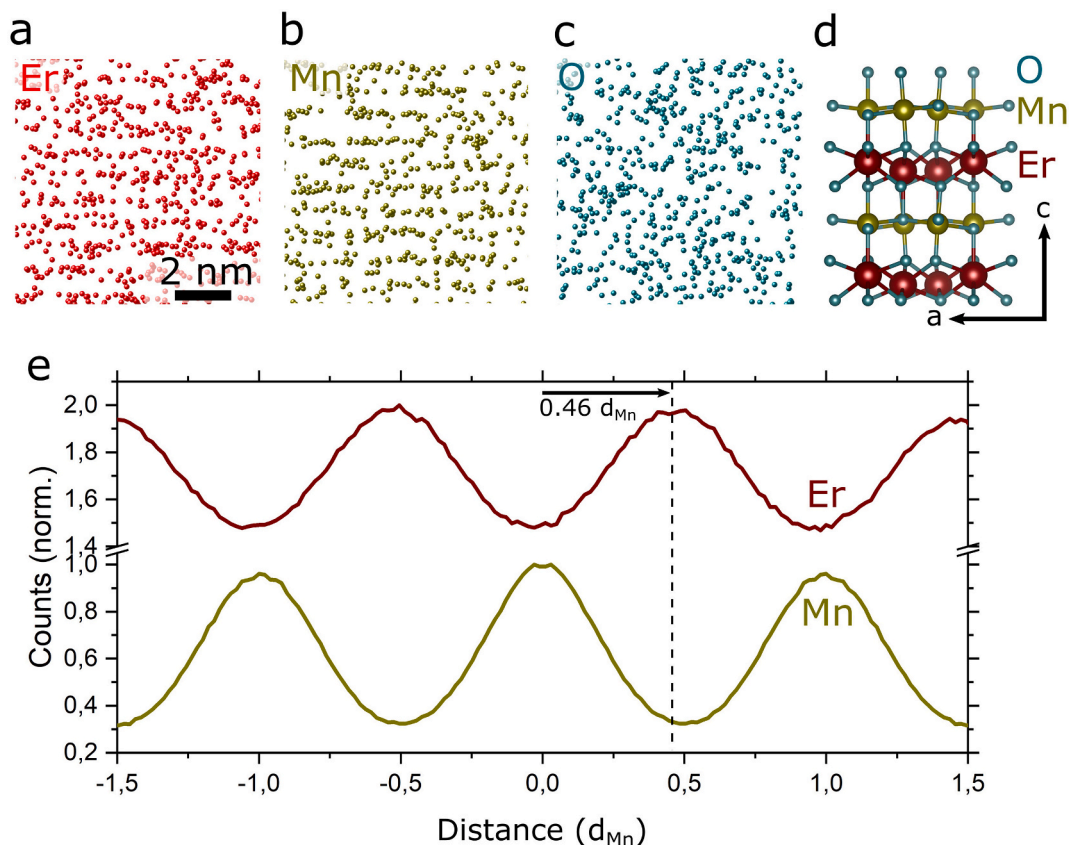
Fig. 4. Atomic resolution in the pole. (a)-(c) Representation of the atomic planes of the three elements, visualized using the main ionic species (i.e., Er and ErO, Mn, O). (d) ErMnO$_3$ unit cell, illustrating the alternating Er and Mn planes. (e) SDM of the main Er and Mn species (Mn – Mn, Mn – Er and ErO), calculated from a selected area from the pole. Mn is used as reference in all cases, and the horizontal axis is given in terms of the Mn-to-Mn peak distance, d_{Mn}, with the direction of evaporation from right to left. The SDMs are normalized with respect to their peak value, and the SDM for Er is shifted vertically by 1 for visualization. Data is taken at 25 K.
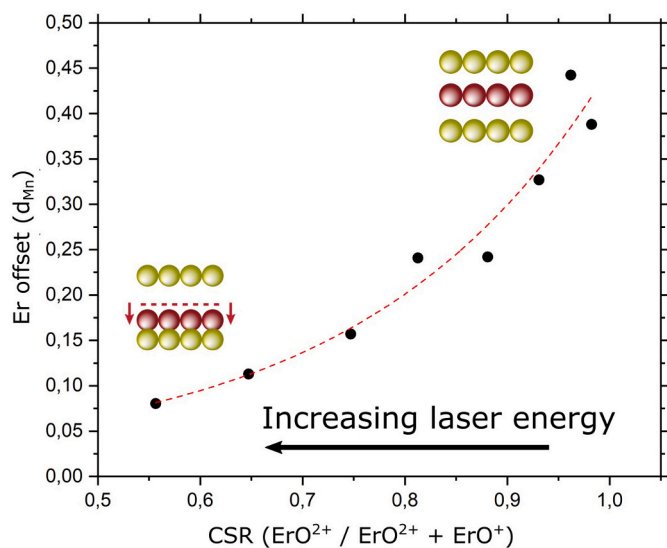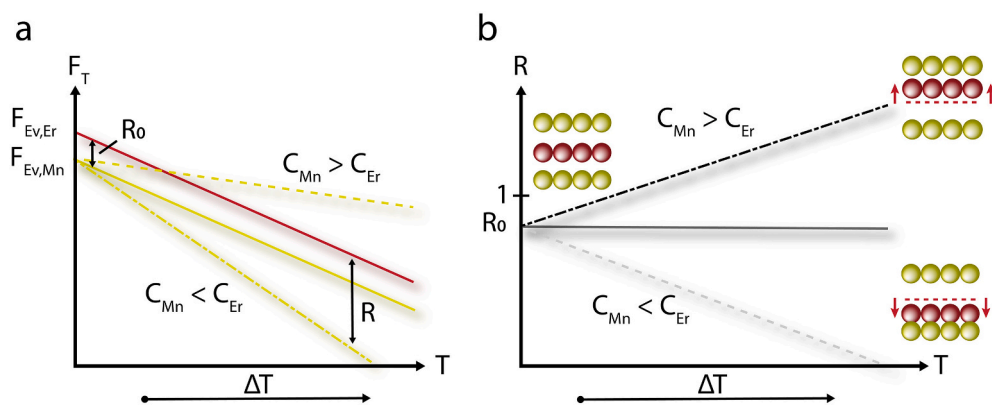

Fig. 5. The Er offset as indicated in Fig. 4(e) plotted against the CSR, where higher values indicate higher electric field strength. The different CSR data points are obtained from the same specimen by varying the laser energy. Atomic offsets are sketched in the plot, where yellow atoms illustrate Mn and red atoms illustrate Er. Data is taken at 50 K. (For interpretation of the references to colour in this figure legend, the reader is referred to the web version of this article.)

composition and structure [13,70,71]. By combining these different expressions, the effective evaporation field ratio of Er ($F_{T,Er}$) and Mn ($F_{T,Mn}$) becomes:

$$\frac{F_{T,Mn}}{F_{T,Er}} = \frac{F_{Ev,Mn}}{F_{Ev,Er}} \times \left(\frac{1 + \frac{k_B T \ln(\gamma)}{C_{Mn}}}{1 + \frac{k_B T \ln(\gamma)}{C_{Er}}} \right) \qquad (3)$$

This ratio reflects the amplitude of the difference between the two species' requirements for field evaporation. Most importantly, it reflects the relation between the temperature and the effective evaporation field differences responsible for the spatial offsets. At zero temperature, the ratio of the effective fields is equal to that of the evaporation fields. As the temperature increases, the ratio changes depending on the two energetic constants (C_{Mn}, C_{Er}). Unfortunately, we do not have values for ErMnO$_3$ to precisely estimate this ratio (in general, such an estimation is possible based on density functional theory calculations as presented, for example, in Ref. [70–72]). Field evaporation simulations at the atomic scale (see Fig. S1)[73–75], however, indicate the validity of the theoretical expression and demonstrate its influence on the observed offset of Er planes from the correct position.

To visualize the relation between the ratio of the evaporation fields ($F_{Ev,Mn}/F_{Ev,Er}$) and the effective ones ($F_{T,Mn}/F_{T,Er}$), and to show how it is controlled by the energetic constants (C_{Er} and C_{Mn}), we sketch the different scenarios in Fig. 6. In Fig. 6(a), we show the effective evaporation field as a function of temperature for Mn and Er for three cases: (i) For $C_{Mn} < C_{Er}$, the effective evaporation field of Mn decreases faster than that of Er, leading to a reduced ratio (Fig. 6(b)). As a consequence, preferential retention of Er arises, which is substantial at high temperatures and remains non-zero towards zero Kelvin. This scenario

Fig. 6. (a) Schematic of the change in effective evaporation field, F_T, as a function of temperature, T, and the laser induced heating ΔT. The energetic constant, C_i, determines the slope and, thus, the ratio, R, between the two elements. (b) Depending on the energetic constant, the ratio between effective evaporation field changes as a function of temperature. At low temperatures, the ratio only depends on the difference in evaporation field, whereas at higher temperature the ratio can both increase or decrease. Atomic retention as a result of the change in effective evaporation field ratio is sketched in (b), where atoms (Er – red, Mn – yellow) are displaced from their correct position marked by the dashed line. (For interpretation of the references to colour in this figure legend, the reader is referred to the web version of this article.)

describes our APT analysis of ErMnO$_3$. (ii) In contrast, for $C_{Mn} > C_{Er}$, the ratio can be reduced to 1 at low temperatures. It grows for higher temperatures, potentially reaching the point where Mn is retained but Er is not. (iii) For $C_{Mn} = C_{Er}$, the ratio of the effective fields is equal to the one of the evaporation fields (at all temperature). It is important to note that this ratio depends on both the element bonding (evaporation field) and temperature and, by extension, on the energy of the laser ($T = T_0 + \Delta T$). The latter implies that the laser energy influences the measured position of the atomic planes (Er offset) as demonstrated in Fig. 5, but the preferential retention originates from the distinct chemical bonding of the two elements.

4. Conclusion

We investigated the impact of varying operation parameters in APT measurements on the complex oxide ErMnO$_3$. Consistent with previous studies on other oxide materials, we observed that low-energy laser pulses (i.e., high CSR) result in a higher MRP and a more accurate composition measurement. By analyzing the atomic planes in the (001) pole, we observed an electric field-dependent shift of the Er planes relative to the Mn planes, which does not match the established unit cell structure of ErMnO$_3$. Based on our theoretical analysis and simulations, we attributed this APT-related effect to preferential retention of Er [20]. Our results provide new insight into the evaporation behavior of atomic planes in oxide materials with noticeably different evaporation fields and their evolution with temperature, advancing the understanding of atomic-scale APT measurements on complex single phase material systems.

Declaration of Competing Interest

Authors note no professional or other personal interest, direct or indirect, in any matter that raises or may raise a conflict with the submission of this manuscript. The sole interest of the submission is to publish the research presented.

Data availability

Data will be made available on request.

Appendix A. Supplementary data

Supplementary data to this article can be found online at https://doi.org/10.1016/j.matchar.2023.113085.

References

[1] P. Dumitraschkewitz, S.S.A. Gerstl, L.T. Stephenson, P.J. Uggowitzer, S. Pogatscher, Clustering in age-Hardenable aluminum alloys, Adv. Eng. Mater. 20 (2018) 1800255, https://doi.org/10.1002/adem.201800255.

[2] B. Gault, A. Chiaramonti, O. Cojocaru-Mirédin, P. Stender, R. Dubosq, C. Freysoldt, S.K. Makineni, T. Li, M. Moody, J.M. Cairney, Atom probe tomography, Nat. Rev. Meth. Primers 1 (2021) 1–30, https://doi.org/10.1038/s43586-021-00047-w.

[3] A.A. El-Zoka, S.H. Kim, S. Deville, R.C. Newman, L.T. Stephenson, B. Gault, Enabling near-atomic–scale analysis of frozen water, Sci. Adv. 6 (2020) eabd6324, https://doi.org/10.1126/sciadv.abd6324.

[4] A. La Fontaine, A. Zavgorodniy, H. Liu, R. Zheng, M. Swain, J. Cairney, Atomic-scale compositional mapping reveals mg-rich amorphous calcium phosphate in human dental enamel, Sci. Adv. 2 (2016) e1601145, doi:10.1126/sciadv.1601145.

[5] S.M. Reddy, D.W. Saxey, W.D.A. Rickard, D. Fougerouse, S.D. Montalvo, R. Verberne, A. van Riessen, Atom probe tomography: development and application to the geosciences, Geostand. Geoanal. Res. 44 (2020) 5–50, https://doi.org/10.1111/ggr.12313.

[6] K.A. Hunnestad, C. Hatzoglou, Z.M. Khalid, P.E. Vullum, Z. Yan, E. Bourret, A.T. J. van Helvoort, S.M. Selbach, D. Meier, Atomic-scale 3D imaging of individual dopant atoms in an oxide semiconductor, Nat. Commun. 13 (2022) 4783, https://doi.org/10.1038/s41467-022-32189-0.

[7] K.A. Hunnestad, J. Schultheiß, A.C. Mathisen, C. Hatzoglou, A.T.J. Van Helvoort, D. Meier, Quantitative 3D mapping of chemical defects at charged grain boundaries in a ferroelectric oxide, arXiv 7491 (2022) 1-14, doi:10.48550/arxiv.2212.07924.

[8] T. Boll, T. Al-Kassab, Y. Yuan, Z.G. Liu, Investigation of the site occupation of atoms in pure and doped TiAl/Ti$_3$Al intermetallic, Ultramicroscopy. 107 (2007) 796–801, https://doi.org/10.1016/j.ultramic.2007.02.011.

[9] W.K. Yeoh, B. Gault, X.Y. Cui, C. Zhu, M.P. Moody, L. Li, R.K. Zheng, W.X. Li, X. L. Wang, S.X. Dou, G.L. Sun, C.T. Lin, S.P. Ringer, Direct observation of local potassium variation and its correlation to electronic inhomogeneity in (Ba$_{1-x}$K$_x$) Fe$_2$As$_2$ pnictide, Phys. Rev. Lett. 106 (2011) 247002, https://doi.org/10.1103/PhysRevLett.106.247002.

[10] T. Rademacher, T. Al-Kassab, J. Deges, R. Kirchheim, Ordering and site occupancy of D0$_3$ ordered Fe$_3$Al-5 at%Cr evaluated by means of atom probe tomography, Ultramicroscopy. 111 (2011) 719–724, https://doi.org/10.1016/j.ultramic.2010.12.009.

[11] S. Meher, R. Banerjee, Partitioning and site occupancy of ta and Mo in co-base γ/γ' alloys studied by atom probe tomography, Intermetallics (Barking). 49 (2014) 138–142, https://doi.org/10.1016/j.intermet.2014.01.020.

[12] C. Cappelli, S. Smart, H. Stowell, A. Pérez-Huerta, Exploring biases in atom probe tomography compositional analysis of minerals, Geostand. Geoanal. Res. 45 (2021) 457–476, https://doi.org/10.1111/ggr.12395.

[13] C. Hatzoglou, S. Rouland, B. Radiguet, A. Etienne, G. Da Costa, X. Sauvage, P. Pareige, F. Vurpillot, Preferential evaporation in atom probe tomography: an analytical approach, Microsc. Microanal. 26 (2020) 689–698, https://doi.org/10.1017/S1431927620001749.

[14] D. Zanuttini, I. Blum, L. Rigutti, F. Vurpillot, J. Douady, E. Jacquet, P.M. Anglade, B. Gervais, Simulation of field-induced molecular dissociation in atom-probe tomography: identification of a neutral emission channel, Phys. Rev. A (Coll Park) 95 (2017), 061401, https://doi.org/10.1103/PhysRevA.95.061401.

[15] B. Gault, D.W. Saxey, M.W. Ashton, S.B. Sinnott, A.N. Chiaramonti, M.P. Moody, D. K. Schreiber, Behavior of molecules and molecular ions near a field emitter, New J. Phys. 18 (2016), 033031, https://doi.org/10.1088/1367-2630/18/3/033031.

[16] D.W. Saxey, Correlated ion analysis and the interpretation of atom probe mass spectra, Ultramicroscopy. 111 (2011) 473–479, https://doi.org/10.1016/j.ultramic.2010.11.021.

[17] M. Müller, B. Gault, G.D.W. Smith, C.R.M. Grovenor, Accuracy of pulsed laser atom probe tomography for compound semiconductor analysis, in: J Phys Conf Ser, IOP Publishing, 2011, p. 012031, https://doi.org/10.1088/1742-6596/326/1/012031.

[18] P.A.J. Bagot, O.B.W. Silk, J.O. Douglas, S. Pedrazzini, D.J. Crudden, T.L. Martin, M. C. Hardy, M.P. Moody, R.C. Reed, An atom probe tomography study of site preference and partitioning in a nickel-based superalloy, Acta Mater. 125 (2017) 156–165, https://doi.org/10.1016/j.actamat.2016.11.053.

[19] T.J. Prosa, S. Strennen, D. Olson, D. Lawrence, D.J. Larson, A study of parameters affecting atom probe tomography specimen survivability, Microsc. Microanal. 25 (2019) 425–437, https://doi.org/10.1017/S1431927615258.

[20] J. Takahashi, K. Kawakami, A quantitative model of preferential evaporation and retention for atom probe tomography, surface and Interface, Analysis. 46 (2014) 535–543, https://doi.org/10.1002/sia.5555.

[21] D.R. Diercks, B.P. Gorman, R. Kirchhofer, N. Sanford, K. Bertness, M. Brubaker, Atom probe tomography evaporation behavior of C-axis GaN nanowires: crystallographic, stoichiometric, and detection efficiency aspects, J. Appl. Phys. 114 (2013), 184903, https://doi.org/10.1063/1.4830023.

[22] H. He, J.E. Halpin, S.R. Popuri, L. Daly, J.-W.G. Bos, M.P. Moody, D.A. MacLaren, P.A.J. Bagot, Atom probe tomography of a cu-doped TiNiSn thermoelectric material: nanoscale structure and optimization of analysis conditions, Microsc. Microanal. (2021) 1–8, https://doi.org/10.1017/s1431927621012162.

[23] C. Cappelli, A. Pérez-Huerta, Effect of crystallographic orientation on atom probe tomography geochemical data? Micron 137 (2020) 102910, https://doi.org/10.1016/j.micron.2020.102910.

[24] A. Vella, B. Mazumder, G. Da Costa, B. Deconihout, Field evaporation mechanism of bulk oxides under ultra fast laser illumination, J. Appl. Phys. 110 (2011) 44321, https://doi.org/10.1063/1.3610523.

[25] F. Tang, M.P. Moody, T.L. Martin, P.A.J. Bagot, M.J. Kappers, R.A. Oliver, Practical issues for atom probe tomography analysis of III-nitride semiconductor materials, Microsc. Microanal. 21 (2015) 544–556, https://doi.org/10.1017/S1431927615000422.

[26] F. Li, T. Ohkubo, Y.M. Chen, M. Kodzuka, K. Hono, Quantitative atom probe analyses of rare-earth-doped ceria by femtosecond pulsed laser, Ultramicroscopy. 111 (2011) 589–594, https://doi.org/10.1016/j.ultramic.2010.12.011.

[27] B. Gault, B. Klaes, F.F. Morgado, C. Freysoldt, Y. Li, F. De Geuser, L.T. Stephenson, F. Vurpillot, Reflections on the spatial performance of atom probe tomography in the analysis of atomic neighborhoods, Microsc. Microanal. (2021) 1–11, https://doi.org/10.1017/s1431927621012952.

[28] T. Prosa, D. Lenz, I. Martin, D. Reinhard, D. Larson, J. Bunton, Evaporation-field differences with deep-UV atom probe tomography, Microsc. Microanal. 27 (2021) 1262–1264, https://doi.org/10.1017/s1431927621004736.

[29] A. Sen, M. Bachhav, F. Vurpillot, J.M. Mann, P.K. Morgan, T.A. Prusnick, J. P. Wharry, Influence of field conditions on quantitative analysis of single crystal thorium dioxide by atom probe tomography, Ultramicroscopy. 220 (2021), 113167, https://doi.org/10.1016/j.ultramic.2020.113167.

[30] M. Bachhav, R. Danoix, F. Danoix, B. Hannoyer, S. Ogale, F. Vurpillot, Investigation of wustite ($Fe_{1-x}O$) by femtosecond laser assisted atom probe tomography, Ultramicroscopy. 111 (2011) 584–588, https://doi.org/10.1016/j.ultramic.2010.11.023.

[31] L. Mancini, N. Amirifar, D. Shinde, I. Blum, M. Gilbert, A. Vella, F. Vurpillot, W. Lefebvre, R. Lardé, E. Talbot, P. Pareige, X. Portier, A. Ziani, C. Davesnne, C. Durand, J. Eymery, R. Butté, J.F. Carlin, N. Grandjean, L. Rigutti, Composition of wide bandgap semiconductor materials and nanostructures measured by atom probe tomography and its dependence on the surface electric field, J. Phys. Chem. C 118 (2014) 24136–24151, https://doi.org/10.1021/jp5071264.

[32] R. Verberne, D.W. Saxey, S.M. Reddy, W.D.A. Rickard, D. Fougerouse, C. Clark, Analysis of natural rutile (TiO_2) by laser-assisted atom probe tomography, Microsc. Microanal. 25 (2019) 539–546, https://doi.org/10.1017/S1431927618015477.

[33] E.A. Marquis, B. Gault, Determination of the tip temperature in laser assisted atom-probe tomography using charge state distributions, J. Appl. Phys. 104 (2008) 84914, https://doi.org/10.1063/1.3006017.

[34] R. Kirchhofer, D.R. Diercks, B.P. Gorman, J.F. Ihlefeld, P.G. Kotula, C.T. Shelton, G. L. Brennecka, Quantifying compositional homogeneity in $Pb(Zr, Ti)O_3$ using atom probe tomography, J. Am. Ceram. Soc. 97 (2014) 2677–2697, https://doi.org/10.1111/jace.13135.

[35] R. Kirchhofer, M.C. Teague, B.P. Gorman, Thermal effects on mass and spatial resolution during laser pulse atom probe tomography of cerium oxide, J. Nucl. Mater. 436 (2013) 23–28, https://doi.org/10.1016/j.jnucmat.2012.12.052.

[36] A. Devaraj, R. Colby, W.P. Hess, D.E. Perea, S. Thevuthasan, Role of photoexcitation and field ionization in the measurement of accurate oxide stoichiometry by laser-assisted atom probe tomography, J. Phys. Chem. Lett. 4 (2013) 993–998, https://doi.org/10.1021/jz400015h.

[37] D. Santhanagopalan, D.K. Schreiber, D.E. Perea, R.L. Martens, Y. Janssen, P. Khalifah, Y.S. Meng, Effects of laser energy and wavelength on the analysis of $LiFePO_4$ using laser assisted atom probe tomography, Ultramicroscopy. 148 (2015) 57–66, https://doi.org/10.1016/j.ultramic.2014.09.004.

[39] M. Karahka, Y. Xia, H.J. Kreuzer, The mystery of missing species in atom probe tomography of composite materials, Appl. Phys. Lett. 107 (2015) 62105, https://doi.org/10.1063/1.4928625.

[40] Y. Xia, M. Karahka, H.J. Kreuzer, Field evaporation of ZnO: a first-principles study, J. Appl. Phys. 118 (2015) 25901, https://doi.org/10.1063/1.4926489/140463.

[42] B.B. Van Aken, T.T.M. Palstra, A. Filippetti, N.A. Spaldin, The origin of ferroelectricity in magnetoelectric $YMnO_3$, Nat. Mater. 3 (2004) 164–170, https://doi.org/10.1038/nmat1080.

[43] M. Li, H. Tan, W. Duan, Hexagonal rare-earth manganites and ferrites: a review of improper ferroelectricity, magnetoelectric coupling, and unusual domain walls, Phys. Chem. Chem. Phys. 22 (2020) 14415–14432, https://doi.org/10.1039/d0cp02195d.

[44] S. Artyukhin, K.T. Delaney, N.A. Spaldin, M. Mostovoy, Landau theory of topological defects in multiferroic hexagonal manganites, Nat. Mater. 13 (2014) 42–49, https://doi.org/10.1038/nmat3786.

[45] D. Meier, J. Seidel, A. Cano, K. Delaney, Y. Kumagai, M. Mostovoy, N.A. Spaldin, R. Ramesh, M. Fiebig, Anisotropic conductance at improper ferroelectric domain walls, Nat. Mater. 11 (2012) 284–288, https://doi.org/10.1038/nmat3249.

[46] J.A. Mundy, J. Schaab, Y. Kumagai, A. Cano, M. Stengel, I.P. Krug, D.M. Gottlob, H. Doğanay, M.E. Holtz, R. Held, Z. Yan, E. Bourret, C.M. Schneider, D.G. Schlom, D.A. Muller, R. Ramesh, N.A. Spaldin, D. Meier, Functional electronic inversion layers at ferroelectric domain walls, Nat. Mater. 16 (2017) 622–627, https://doi.org/10.1038/nmat4878.

[47] S.H. Skjærvø, E.T. Wefring, S.K. Nesdal, N.H. Gaukås, G.H. Olsen, J. Glaum, T. Tybell, S.M. Selbach, Interstitial oxygen as a source of p-type conductivity in hexagonal manganites, Nat. Commun. 7 (2016) 13745, https://doi.org/10.1038/ncomms13745.

[48] P. Liu, X.L. Wang, Z.X. Cheng, Y. Du, H. Kimura, Structural, dielectric, antiferromagnetic, and thermal properties of the frustrated hexagonal $Ho_{1-x}Er_xMnO3$ manganites, Phys. Rev. B Condens. Matter. Mater. Phys. 83 (2011), 144404, https://doi.org/10.1103/PhysRevB.83.144404.

[49] S.H. Skjærvø, D.R. Småbråten, N.A. Spaldin, T. Tybell, S.M. Selbach, Oxygen vacancies in the bulk and at neutral domain walls in hexagonal $YMnO_3$, Phys. Rev. B 98 (2018), 184102, https://doi.org/10.1103/PhysRevB.98.184102.

[50] Z. Yan, D. Meier, J. Schaab, R. Ramesh, E. Samulon, E. Bourret, Growth of high-quality hexagonal $ErMnO_3$ single crystals by the pressurized floating-zone method, J. Cryst. Growth 409 (2015) 75–79, https://doi.org/10.1016/j.jcrysgro.2014.10.006.

[51] K. Thompson, D. Lawrence, D.J. Larson, J.D. Olson, T.F. Kelly, B. Gorman, In situ site-specific specimen preparation for atom probe tomography, Ultramicroscopy. 107 (2007) 131–139, https://doi.org/10.1016/j.ultramic.2006.06.008.

[52] F. Meisenkothen, T.F. Kelly, E. Oltman, J.H. Bunton, L. Renaud, D.J. Larson, Using mass resolving power as a performance metric in the atom probe, Microsc. Microanal. 22 (2016) 680–681, https://doi.org/10.1017/s1431927616004256.

[53] C. Hatzoglou, Norwegian Atom Probe App, 2023.

[54] T. Choi, Y. Horibe, H.T. Yi, Y.J. Choi, W. Wu, S.W. Cheong, Insulating interlocked ferroelectric and structural antiphase domain walls in multiferroic $YMnO_3$, Nat. Mater. 9 (2010) 253–258, https://doi.org/10.1038/nmat2632.

[55] M.E. Holtz, K. Shapovalov, J.A. Mundy, C.S. Chang, Z. Yan, E. Bourret, D.A. Muller, D. Meier, A. Cano, Topological defects in hexagonal Manganites: inner structure and emergent electrostatics, Nano Lett. 17 (2017) 5883–5890, https://doi.org/10.1021/acs.nanolett.7b01288.

[57] Q.H. Zhang, L.J. Wang, X.K. Wei, R.C. Yu, L. Gu, A. Hirata, M.W. Chen, C.Q. Jin, Y. Yao, Y.G. Wang, X.F. Duan, Direct observation of interlocked domain walls in hexagonal $RMnO_3$ (R=tm, Lu), Phys. Rev. B Condens. Matter. Mater. Phys. 85 (2012) 20102, https://doi.org/10.1103/PhysRevB.85.020102.

[58] S.-H. Yoo, S.-H. Kim, E. Woods, B. Gault, M. Todorova, J. Neugebauer, Origins of the hydrogen signal in atom probe tomography: case studies of alkali and noble metals, New J. Phys. (2021), https://doi.org/10.1088/1367-2630/ac40cd.

[59] D.R. Kingham, The post-ionization of field evaporated ions: a theoretical explanation of multiple charge states, Surf. Sci. 116 (1982) 273–301, https://doi.org/10.1016/0039-6028(82)90434-4.

[60] N. Amirifar, R. Lardé, E. Talbot, P. Pareige, L. Rigutti, L. Mancini, J. Houard, C. Castro, V. Sallet, E. Zehani, S. Hassani, C. Sartel, A. Ziani, X. Portier, Quantitative analysis of doped/undoped ZnO nanomaterials using laser assisted atom probe tomography: influence of the analysis parameters, J. Appl. Phys. 118 (2015), 215703, https://doi.org/10.1063/1.4936167.

[61] B. Gault, M. Moody, J. Cairney, S. Ringer, Atom probe tomography, Springer, New York, NY, 2012.

[62] B. Gault, F. Danoix, K. Hoummada, D. Mangelinck, H. Leitner, Impact of directional walk on atom probe microanalysis, Ultramicroscopy. 113 (2012) 182–191, https://doi.org/10.1016/j.ultramic.2011.06.005.

[63] B.P. Geiser, T.F. Kelly, D.J. Larson, J. Schneir, J.P. Roberts, Spatial distribution maps for atom probe tomography, Microsc. Microanal. 13 (2007) 437–447, https://doi.org/10.1017/S1431927607070948.

[64] F. Vurpillot, A. Bostel, E. Cadel, D. Blavette, The spatial resolution of 3D atom probe in the investigation of single-phase materials, Ultramicroscopy. 84 (2000) 213–224, https://doi.org/10.1016/S0304-3991(00)00035-8.

[65] E.W. Müller, Field desorption, physical, Review. 102 (1956) 618–624, https://doi.org/10.1103/PhysRev.102.618.

[66] M.K. Miller, R.G. Forbes, Atom Probe Tomography, Elsevier, 2009, https://doi.org/10.1016/j.matchar.2009.02.007.

[67] F. Williams Lefebvre, X. Sauvage Vurpillot, Atom Probe Tomography, Elsevier, London, 2016, https://doi.org/10.1016/B978-0-12-804647-0.00008-5. https://www.sciencedirect.com/book/9780128046470/atom-probe-tomography.

[68] R.G. Forbes, Field evaporation theory: a review of basic ideas, Appl. Surf. Sci. 87–88 (1995) 1–11, https://doi.org/10.1016/0169-4332(94)00526-5.

[69] G.L. Kellogg, Measurement of activation energies for field evaporation of tungsten ions as a function of electric field, Phys. Rev. B 29 (1984) 4304–4312, https://doi.org/10.1103/PhysRevB.29.4304.

[70] T. Carrasco, J. Peralta, C. Loyola, S.R. Broderick, Modeling field evaporation degradation of metallic surfaces by first principles calculations: a case study for Al, Au, Ag, and Pd, J. Phys. Conf. Ser. 1043 (2018), 012039, https://doi.org/10.1088/1742-6596/1043/1/012039.

[71] J. Peralta, S.R. Broderick, K. Rajan, Mapping energetics of atom probe evaporation events through first principles calculations, Ultramicroscopy. 132 (2013) 143–151, https://doi.org/10.1016/j.ultramic.2013.02.007.

[72] T. Ohnuma, Surface diffusion of Fe and cu on Fe (001) under electric field using first-principles calculations, Microsc. Microanal. 25 (2019) 547–553, https://doi.org/10.1017/S1431927618015738.